Inversion of dislocation loop nature driven by cluster migration in self-ion irradiated nickel

Kan Ma, Brigitte Décamps, Anna Fraczkiewicz, Frédéric Prima, Marie Loyer-Prost

Inversion of dislocation loop nature driven by cluster migration in self-ion irradiated nickel

Kan MA[a,d,1], Brigitte DÉCAMPS[b], Anna FRACZKIEWICZ[c], Frédéric PRIMA[d] and Marie LOYER-PROST[a*].

[a]Université Paris-Saclay, CEA, Service de Recherches de Métallurgie Physique, Gif-sur-Yvette, France;

[b]Laboratoire de Physique des 2 infinis Irène Joliot-Curie (IJCLab), Université Paris-Saclay, Orsay, France;

[c]MINES Saint-Etienne, Université de Lyon, CNRS, UMR 5307 LGF, Centre SMS, 42023, Saint-Etienne, France;

[d]PSL Research University, Chimie ParisTech-CNRS, Institut de Recherche de Chimie Paris, Paris, France.

[1]Currently at the School of Metallurgy and Materials, University of Birmingham B15 2TT, United Kingdom.

*Corresponding author: Marie LOYER-PROST.

Mail: marie.loyer-prost@cea.fr

Courrier: CEA Saclay, DES/ISAS/DMN/SRMP/JANNUS (Bât 126, pièce 58), PC. 162, 91191 Gif-sur-Yvette CEDEX, France.

Telephone +33 (0)1 69 08 24 68.

Abstract

Nickel is widely used as fcc model material to obtain insight into fundamental mechanisms of radiation damage. This work presents irradiation of high-purity nickel using self-ions at 450°C and fine analysis of dislocation loops in specimens prepared by Focus Ion Beam using Transmission Electron Microscopy. For the first time to our knowledge, an inversion of loop nature (vacancy-type in irradiated zones v.s. interstitial-type in unirradiated zones) and a change of loop Burgers vector (1/3<111> and 1/2<110> loops v.s. only 1/2<110> loops) is identified along the implantation direction in irradiated nickel. This change may be attributed to the formation of interstitial <110> crowdions and their long-range one-dimension migration. A defect-free layer related to the annihilation of vacancy defects by injected atoms is detected. . It allows the identification of the injection peak which is uncommon for self-ion irradiated specimens and validates the damage calculations.

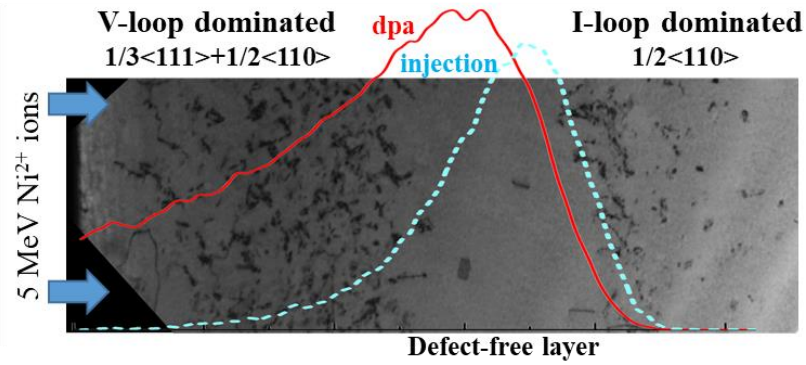

5 keywords

Nickel, microstructure, dislocation, TEM, radiation damage

Novel austenitic materials [1,2] and single-phase concentrated solid-solution alloys including high entropy alloys (HEA) [3,4] are new classes of face-cubic centered (fcc) metallic materials. They display exceptional improvement of radiation-resistance compared to traditional fcc materials thus are promising candidates for future nuclear applications [5,6]. However, their reliability under irradiation requires further examinations and a better understanding of the fundamental mechanisms of radiation damage in the fcc structures.

For this purpose, pure nickel (Ni) and Ni-based alloys are widely used as fcc model materials to investigate radiation-induced defects and solute effects [7–10]. The irradiation behavior of Ni as a reference system draws particular attention. Radiation-induced dislocation loops were detected as a characteristic defect in the early stage of irradiation in Ni [7,9,11,12]. Therefore, the loop formation and evolution were largely studied over a wide range of temperatures and doses in Ni [9,13–17]. The same interstitial nature of loops was identified in most of experiments. The stability of interstitial loops and their growth mechanism under irradiation were explained by the dislocation bias model in which dislocation lines/loops absorb preferentially interstitial atoms [13,14]. Nevertheless, recently, vacancy-type loops were identified for the first time as dominant in the microstructure, within the damage zones of Ni irradiated by self-ions at 450°C [18]. The same vacancy nature was identified in as-irradiated TEM thin foils [19] and Focus Ion Beam (FIB) specimens up to 1.5 µm irradiation depth [18]. Interstitial Frank loops were only occasionally detected within vacancy-type Frank loops eradicating the outer vacancy loop [18]. These observations contrasts with the well-established interstitial loop nature in literature and could be explained by the high mobility of interstitial clusters escaping from the damage production zone [9,19–21]. To better elucidate the mechanisms, full characterization of dislocation loops (their nature and type) along the ion irradiation profile is therefore essential and has never been explored in ion-irradiated Ni.

In this work, ultra-high-purity nickel is manufactured by cold crucible induction melting at the Ecole des Mines de Saint Etienne with measured impurities in mass ppm: O<2, C<8, N<2, S<2. 3 mm diameter foils are irradiated at the JANNuS-Saclay platform using a raster beam of 5

MeV Ni^{2+} ions at 450°C up to $2.3x10^{15}$ ions.cm^{-2}. Dislocation loops and their nature are investigated from the surface up to 3 µm depth. The radiation damage is calculated using the Stopping and Range of Ions in Matter 2013 code (SRIM) [22] and IRADINA [23] in Kinchin–Pease mode with a displacement threshold energy of 40 eV. Good agreement is obtained between two codes and the damage profile by SRIM is shown in Fig. 1(a). The dose is about 0.7 dpa at the surface and 2.2 dpa at the damage peak. Cross-sectional samples are lifted-out using FIB equipped on an FEI Helio 650 NanoLab dual-beam Scanning Electron Microscopy (SEM) followed by a flash polishing technique [24] to remove FIB-induced damage. The irradiated microstructure in FIB specimens is characterized with a 200 kV FEI TECNAI G2 TEM. Conventional TEM techniques are applied to characterize dislocation loops using invisibility criterion [25] and inside-outside method [26–28] respectively for the determination of loop Burgers vectors and natures under Finish-Start/Right-Hand convention [29].

Fig. 1(a) presents the typical panorama obtained for irradiated microstructures with the damage and injection profiles. The damage and injection peaks are respectively at 1.5 µm and 1.8 µm in depth. Dislocation loops are the main defect formed in the microstructure. Only two voids are detected in the specimen and their density is neglected. Some small defects (<5 nm) are detected. Some of them exhibit a triangle form so could be Staking Fault Tetrahedrons (SFT) (Fig. S1 in supplementary materials). Generally, it is difficult to distinguish them from loop to SFT. In this work, we will focus on the dislocation loops and lines as they are dominating the microstructure. The average loop size, loop density and dislocation line density are measured and plotted in Fig. 1(e). A strong heterogeneity of the defect distribution is thus revealed as observed in Fig. 1(a). Similar phenomenon is observed in other samples with different orientations (Fig. S2 in supplementary materials).

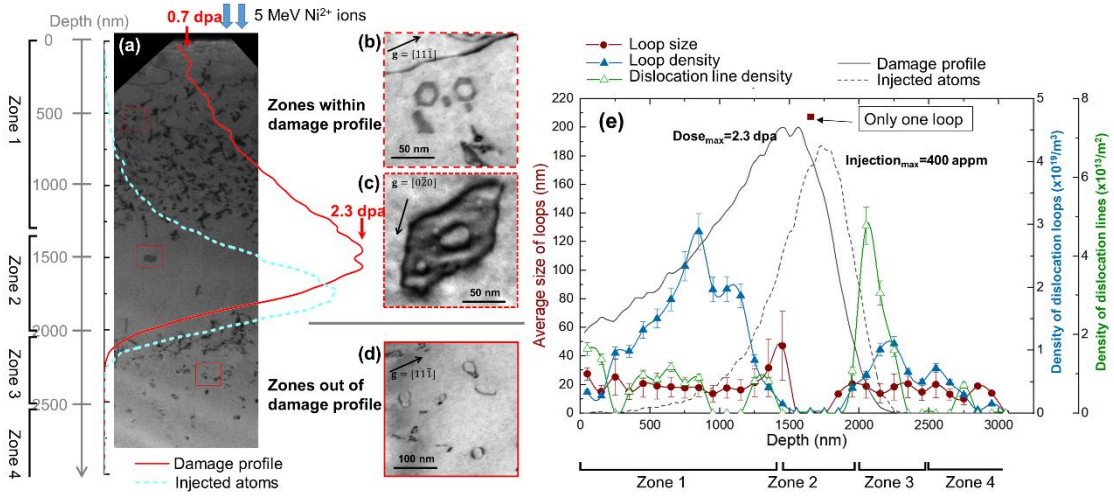

Fig. 1 Microstructure irradiated up to 2.3x10^{15} ions.cm-^{2} at 450°C: (a) Low magnification Bright-Field (BF) TEM micrograph image showing the general microstructure with the damage profile and injected atoms calculated using SRIM-2013; (b-c) BF images of two typical Frank loops at depth ≤ 1.5 µm with diffraction vectors g indicated by black arrows; (d) BF images of perfect loops outside the damage profile; (e) depth-dependency of the average size and density of loops as well as the density of dislocation lines.

The microstructure can be divided into four zones. The first damaged zone (0-1.3 µm) is within the damage profile with limited injected atoms. In this zone, both Frank loops and perfect loops are detected. Fig. 1(b) shows some typical single-layer and double-layer Frank loops in this zone. In fact, all single-layer Frank loops and the outer loops of double-layer ones are vacancy-type and segmented as shown in Fig. 2. Multiple ±g pairs are used and the same results are obtained.

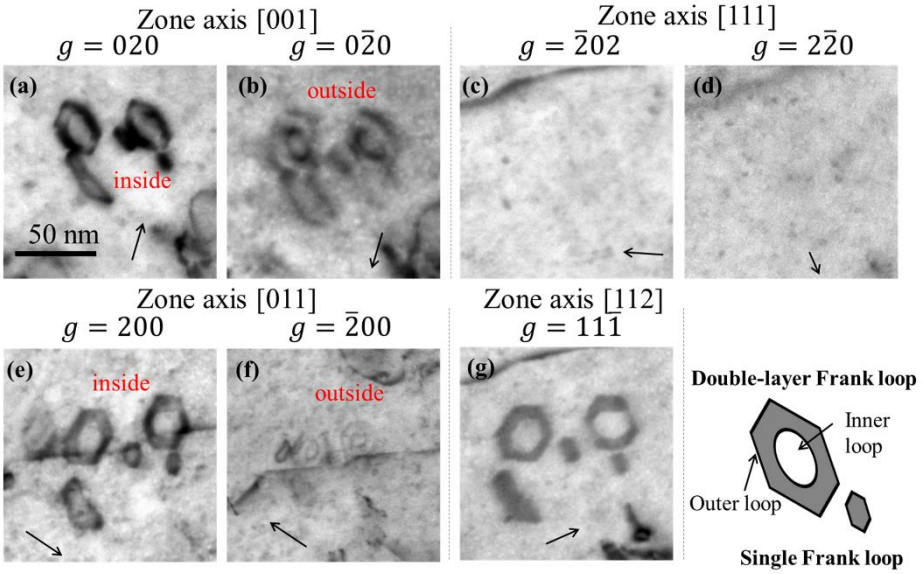

(h)

Loops	Contrast of loops (zone axis [001])			**g.b** for +**g**	**b**	Nature
	b direction	+**g**=[020]	-**g**=[0$\bar{2}$0]			
Single loop / Outer loop	[111]	inside	outside	<0	[$\bar{1}\bar{1}\bar{1}$]	vacancy
Inner loop	[111]	outside	inside	>0	[111]	interstitial

(i)

Loops	Contrast of loops (zone axis [011])			**g.b** for +**g**	**b**	Nature
	b direction	+**g**=[200]	-**g**=[$\bar{2}$00]			
Single loop / Outer loop	[111]	inside	outside	<0	[$\bar{1}\bar{1}\bar{1}$]	vacancy
Inner loop	[111]	outside	inside	>0	[111]	interstitial

Fig. 2 Determination of the Burgers vectors of the Frank loops in thin foil Ni irradiated at 450°C within the damage profile: (a-g) Bright-field TEM images of the Frank loop under different two-beam conditions with diffraction vector **g** indicated by arrows with the same scale bar in (a); (h) and (i) tables of loop nature determination based on two $\pm$g pairs using the inside-outside method [27].

Fig. 2 displays the determination of both Burgers vector and nature of Frank loops. Their Burgers vector is identified as $\pm a_0/3[111]$ (see Table S.1 in the supplementary material) as they are invisible with g=[$\bar{2}$02] and g=[2$\bar{2}$0] (**g**.**b**=0). Their inside-outside behavior is summarized in Fig. 2(f), leading to a Burgers vector of $a_0/3[\bar{1}\bar{1}\bar{1}]$. As the loop plan normal **n** and the Burgers vector **b** are pointing in opposite directions, i.e. **n**.**b**<0, they are vacancy-type loops. The inner loops are also Frank loops but interstitial-type, so they eradicate the stacking fault of the outer loop, which was analyzed in details in [18]. Meanwhile, the same nature of perfect loops is also observed within the zone. Fig. 3 presents the determination of loop nature for a typical perfect

loop within the damage zone. The outer loop and inner loops are coplanar as they are almost superposed in the edge-on position in Fig. 3(a). Their habit plane is thus close to (110), i.e. **n**≈[110]. From their visibility (Table S.1) and inside-outside behavior (for **g**=±[200] close to the zone axis [011]), their Burgers vector is $a_0[\bar{1}\bar{1}0]$, resulting in vacancy nature as **n**.**b**<0. Besides, they are close to edge position. Overall, only vacancy loops are detected in the first damage zone. The second zone (1.3-2.0 μm) is the overlap of the damage and injection profile. This layer is almost defect-free: only one vacancy-type Frank large loop is detected as shown in Fig. 1(c).

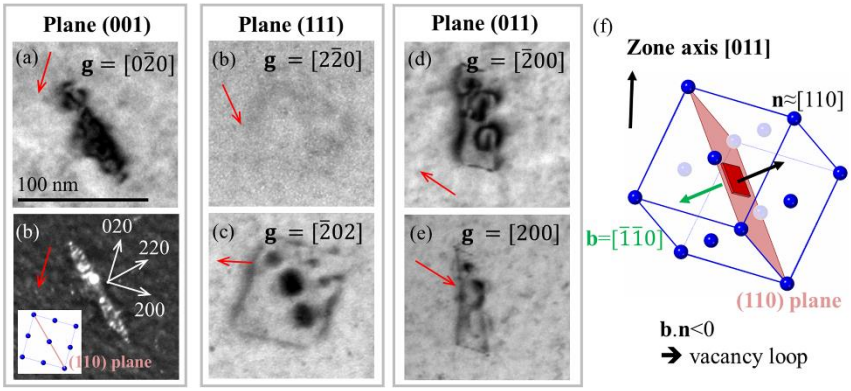

Fig. 3 Determination of the Burgers vector of perfect loops in thin foil Ni irradiated at 450°C within the damage profile: (a-e) TEM images of the Frank loop under different two-beam conditions with diffraction vector **g** indicated by red arrows with the same scale bar in (a); (f) Geometry of the crystal orientation, loop plane and loop Burgers vector to determine the loop nature using the inside-outside method [27].

The third zone (2.0-2.5 μm) is outside the irradiated depth. This layer is dominated by dislocation lines and loops. It is interesting to note that no stacking fault contrast is detected in most loops in this zone as shown in Fig. 1(d) though some loops are too small (<5 nm) to confirm. Then, the type and nature of loops in the second damage zone is determined. Fig. 4(a-g) present a representative zone at about 2.2 μm depth under different diffraction conditions. The diffraction vector **g** for each micrograph is indicated by the black arrow. Five typical loops (A, B, C, D and E) are chosen to show the determination of loop nature. For each **g**, red circles point out the position of these loops. When a loop is invisible, the circle is dashed. A visibility table is made for used **g** and the Burgers vector for each loop is analyzed in Fig. 4(i) and they are all perfect loops.

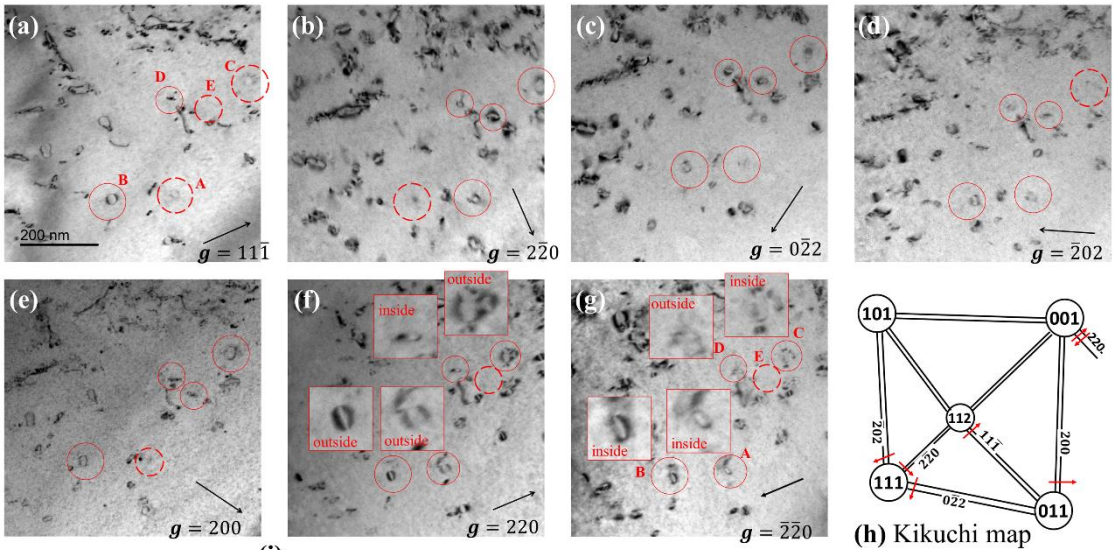

(i)

Table of visibility (V= visible, I= invisible)	Zone axes	[112]	[111]			[011]	[001]		Loop
	g / Possible b	11$\bar{1}$	2$\bar{2}$0	0$\bar{2}$2	$\bar{2}$02	200	220	2$\bar{2}$0	
	$\pm\frac{1}{2}$[110]	V	I	V	V	V	V	V	B
	$\pm\frac{1}{2}$[$\bar{1}$10]	I	V	V	V	V	I	I	E
	$\pm\frac{1}{2}$[101]	I	V	V	I	V	V	V	C
	$\pm\frac{1}{2}$[10$\bar{1}$]	V	V	V	V	V	V	V	D
	$\pm\frac{1}{3}$[011]	I	V	I	V	I	V	V	A
	$\pm\frac{1}{3}$[01$\bar{1}$]	V	V	V	V	I	V	V	

(j)

Loops	Contrast of loops along zone axis [001]				**g** · **b** for **g**	**b**	Nature
	Safe?	**b** direction	**g** = [220]	−**g** = [2$\bar{2}$0]			
A	safe	[011]	outside	inside	>0	1/2 [011]	interstitial
B	unsafe	[110]	/	/	/	/	/
C	safe	[101]	outside	inside	>0	1/2 [101]	interstitial
D	safe	[10$\bar{1}$]	inside	outside	<0	1/2 [$\bar{1}$01]	interstitial
E	unsafe	[$\bar{1}$10]	/	/	/	/	/

Fig. 4 Determination of the perfect loop nature out of the damage production zones in Ni irradiated 450°C to 2.3x10^{15} ions.cm^{-2}: (a-h) Bright-field TEM images of irradiated Ni under ten two-beam conditions along different zone axis; diffraction vector **g** indicated by black arrow in each micrograph with the same scale bar for all images in (a); (i) table of visibility based on **g**.**b** value; (j) determination of loop nature based on inside-outside contrast in (f) and (g).

The inside-outside method with safe/unsafe condition is used to determine the nature of these perfect loops [27,28]. According to the method, the nature of a perfect loop can only be determined if the loop is under safe conditions. In the fcc structure, for a given observation zone axis, a perfect loop is under safe condition if the angle α between its Burgers vector $\mathbf{b_p}$ and the zone axis **z** satisfies α<(90°-35°)=55°. In Fig. 4, an inside-outside pair (±**g**) is chosen along the zone axis [001] with **g**=±[220]. The angle α for the Burgers vectors A, B, C, D, E (Fig. 4(i)) are respectively close to 45/90/45/45/90°: loops A, C and D are under safe conditions. Fig. 4(j) presents the inside-outside analysis for loops under safe conditions (A, C and D). From their inside-outside behavior, loop A, C and D are interstitial-type. Other loops at depth > 2.0 µm are analyzed and the same interstitial-nature is identified. Thus, we assume that the microstructure in

this layer is dominated by interstitial-type perfect loops. The fourth zone (beyond the 2.5 μm depth) is free of radiation-induced defects.

Based on these thorough and local analysis of dislocation loops, the global picture of microstructure in Ni irradiated in the studied conditions is unambiguously revealed. The microstructure appears to be dominated by vacancy-type Frank loops and perfect loops up to 1.3 μm depth, followed by a defect-free layer corresponding to the injection profile. Then, a layer outside the damage profile is dominated by interstitial-type perfect loops. To our knowledge, a drastic change of loop nature (vacancy-type v.s. interstitial-type) and loop type (both Frank and perfect loops v.s. only perfect loops) along the depth direction is for the first time identified in irradiated Ni. It is critical to understand the origin of the change of loop nature and type.

In terms of loop nature, it is recognized that interstitial loops should grow under irradiation while vacancy loops should rather shrink. All loops have indeed a positive bias with the assumption that free migrating interstitials and vacancies are equally accessible to loops [30]. However, in this work, the vacancy loop dominated microstructure suggests strong excess of vacancies/vacancy clusters (V-clusters) in irradiated zones (0 to 1.3 μm depth in Fig. 1). A plausible explanation of the vacancy excess is that interstitial clusters (I-clusters) are highly mobile and can escape from the production zone, either to the surface or to unirradiated zones while V-clusters are less mobile and remain within their production zone. This mechanism has been studied by theoretical calculations [9,20,21]. Some I-clusters in the fcc structure were suggested to be highly mobile and to migrate in long-range 1D motion while V-clusters have low mobility [20,31,32]. In our previous work [19], the microstructure of irradiated thin foil Ni was dominated by vacancy loops. Rate theory combined with an original production bias model was suggested to explain the vacancy nature of loops. In the model, I-clusters formed within cascades are assumed to be partially (about 10% for 260 nm thickness at 510°C [19]) absorbed by free surfaces due to their high mobility, which can theoretically lead to the growth of vacancy loops. The observation in this work (vacancy loops present up to 1.5 μm in depth) demonstrates that the

migration distance of I-clusters is much larger than the scale of thin foil thickness (~200 nm). I-clusters can migrate either to the surface or deeply in the material.

The stability of vacancy loops over SFT or voids may raise questions. In previous studies, the relative stability of vacancy defects was investigated [18,33]. They revealed that in certain cases, loops can indeed be the stable form. The average number of vacancies present in loops in this study (~20nm in diameter giving 6.10^3 vacancies) is within the range of vacancy loop domination [18]. Nevertheless, the variation of loop types observed in our sample (vacancy Frank and perfect loops up to 1.5 µm v.s. interstitial perfect loops above 2.0 µm) can be hardly explained with only the 1D motion of I-clusters. Further mechanism should be involved to understand why there are only perfect loops in unirradiated zones. A key factor is the difference among various type of clusters. It is well known that, in fcc structure, I-clusters formed within the cascades are in form of <100> dumbbells, <110> crowdions (perfect-loop-like clusters) or clusters with stacking fault (Frank-loop-like clusters) [31,32,34,35]. They have different mobility: <110> crowdions glide fast in 1D along their axis direction (<110> directions) while <100> dumbbells display usually short-range 3D motion and defects with stacking fault are sessile. Moreover, it is worth noting that interstitial <100> dumbbells are reported to be unstable for T>426°C (700 K) and to transform into interstitial <110> crowdions [35]. These subtle differences of cluster mobility and stability give a natural explanation of both loop type and nature (interstitial-type perfect loops) in unirradiated zones. <110> perfect-loop-like crowdions could be formed directly within the cascades or from the transformation of <100> dumbells, then they escape out of their production zones, resulting in a vacancy excess in the irradiated zones and an interstitial-perfect-loop dominated zone outside.

In our experiments, interstitial Frank loops are preferentially nucleated within large vacancy Frank loops as they provide a dilatation zone. Independent interstitial Frank loops are not detected outside vacancy loops. Indeed, newly nucleated Frank loops formed within cascades would shrink and disappear due to the excess of vacancies.

The defect-free layer (1.3 to 2.0 μm depth in Fig. 1) between the two loop-dominated zones is also of great interest to study the injection peak. The injection profile is essential to reveal the depth-dependency of radiation damage and calibrate damage calculation codes such as SRIM and IRADINA. Generally, it is tricky to probe the implantation profile in self-ion irradiated materials. Nevertheless, in this work, we can detect the damage peak using the defect-free layer. In fact, we assumed that the injected interstitials compensate the interstitial loss due to 1D migration leading to the defect-free layer. The injected atoms compensate partially the interstitial loss, inducing a strong annihilation of vacancy loops in this zone. Hence, the injection peak prevents the growth and gliding of vacancy <110> crowdions and 1/2<110> loops. Therefore, the depth of the defect-free layer should correspond to this peak. For the first time to our knowledge, these results allow to experimentally identify the injection peak in self-ion irradiated specimens, providing precious experiment data to validate the calculation of radiation damage with dedicated codes (e.g., SRIM and IRADINA). The experimental validation of calculated implantation profiles is an important topic within the community as the phenomenal interpretation on radiation damage is closely related to them, e.g. in [36]. Furthermore the topic is particularly important for Ni as the calculated profiles differ from SRIM and Iradina to the formerly used codes (TRIM98, Brice)[37]. The observed defect free layer can not only be explained by an increase of defect recombination due to a higher damage rate at the damage peak (2.7 $x10^{-4}$ dpa/s). Indeed, past experiment realized with the same damage rate shows that vacancy loops grow at this level of flux [19]. Therefore, the observed defect free layer is related to the implantation peak. Nevertheless, it observed here needs further understanding as the implanted ions at the injection peak, equal to $4x10^{-4}$ appm (Figure 1(e)), does not compensate for the predicted loss of interstitials, equal to $6x10^{-3}$ appm (1.5 dpa x 4% displacement efficiency [38] x 10% loss percent [19]), based on the actual knowledge of the material. The accuracy of the real defect production rate or/and the survival defect proportion in cascades is thus questioned. These parameters are critical to correctly predict and understand the properties of any material under any type of irradiation.

Last, it is worth noting the high dislocation density at ~2.1 μm depth (Fig. 1(e)) outside the damage profile. A plausible explanation is that the migration of clusters and loops (created in irradiated zones) is enhanced by cascade damage [39]. Once they move into unirradiated zones, their mobility reduces strongly so the majority remain at this depth leading to the loop agglomeration.

In summary, fine microstructural analysis is performed in FIB-lifted Ni specimens irradiated by self-ion at 450°C. The present findings lead to the following conclusions:

(1) For the first time, a drastic change of loop nature (vacancy-type v.s. interstitial-type) and loop type (Frank and perfect loops v.s. only perfect loops) is identified. Within the irradiated zone, the vacancy-loop-dominated microstructure is observed related to an excess of vacancies while the interstitial-perfect-loop-dominated layer is detected in deep zones. All vacancy Frank loops are segmented confirming the strong correlation between the loop morphology and its nature [18,19]. This vacancy excess in irradiated zones results from the migration of interstitial defects away from the damage zone. The formation of interstitial <110> crowdions and their long-range 1D motion could be the key mechanism leading to this change.

(2) A defect-free layer is formed between the two loop-dominated zones and should correspond to the peak of injected self-interstitial atoms. This observation allows the identification of the injection peak which is very uncommon in self-ion irradiated metals without injecting impurities. Moreover, the good agreement between the depth of the defect-free layer and the depth of injection peak using SRIM and IRADINA offers precious validation for both codes.

Acknowledgments

The research was supported by the Cross-cutting basic research Program of Division Energy of CEA (RTA Program), the RMATE project (CEA), the NEEDS program (CNRSCEA-EDF-ANDRA-AREVA-IRSN-BRGM) and by the French government, managed by the French National Research Agency, under the ‘Investissements d’avenir’ program (No. ANR-11-EQPX-

0020). The support of JANNuS-Saclay-CEA team is acknowledged by authors for the ion irradiation experiments. Also, the useful help of P. XIU and C. LU for the flash polishing is acknowledged.

Reference

[1] P. Yvon, Structural Materials for Generation IV Nuclear Reactors, 1st ed., Woodhead Publishing, United Kingdoms, 2016.
[2] S.J. Zinkle, G.S. Was, Acta Materialia 61 (2013) 735–758.
[3] D.B. Miracle, O.N. Senkov, Acta Materialia 122 (2017) 448–511.
[4] B. Gludovatz, A. Hohenwarter, D. Catoor, E.H. Chang, E.P. George, R.O. Ritchie, Science 345 (2014) 1153–1158.
[5] S.J. Zinkle, J.T. Busby, Materials Today 12 (2009) 12–19.
[6] X. Yan, Y. Zhang, Scripta Materialia 187 (2020) 188–193.
[7] S.I. Porollo, A.M. Dvoriashin, Yu.V. Konobeev, F.A. Garner, Journal of Nuclear Materials 442 (2013) S809–S812.
[8] T. Yoshiie, Q. Xu, Y. Satoh, H. Ohkubo, M. Kiritani, Journal of Nuclear Materials 283–287 (2000) 229–233.
[9] C. Lu, L. Niu, N. Chen, K. Jin, T. Yang, P. Xiu, Y. Zhang, F. Gao, H. Bei, S. Shi, M.-R. He, I.M. Robertson, W.J. Weber, L. Wang, Nature Communications 7 (2016) 13564.
[10] C. Lu, T. Yang, L. Niu, Q. Peng, K. Jin, M.L. Crespillo, G. Velisa, H. Xue, F. Zhang, P. Xiu, Journal of Nuclear Materials 509 (2018) 237–244.
[11] S.J. Zinkle, L.L. Snead, Journal of Nuclear Materials 225 (1995) 123–131.
[12] S. Kojima, T. Yoshiie, M. Kiritani, Journal of Nuclear Materials 155 (1988) 1249–1253.
[13] K. Urban, Physica Status Solidi (a) 4 (1971) 761–772.
[14] M. Kiritani, N. Yoshida, H. Takata, Y. Maehara, Journal of the Physical Society of Japan 38 (1975) 1677–1686.
[15] S. Ishino, Journal of Nuclear Materials 251 (1997) 225–236.
[16] K. Niwase, T. Ezawa, T. Tanabe, M. Kiritani, F.E. Fujita, Journal of Nuclear Materials 203 (1993) 56–66.
[17] T. Yoshiie, S. Kojima, Y. Satoh, K. Hamada, M. Kiritani, Journal of Nuclear Materials 191–194 (1992) 1160–1165.
[18] K. Ma, B. Décamps, A. Fraczkiewicz, F. Prima, M. Loyer-Prost, Materials Research Letters 8 (2020) 201–207.
[19] K. Ma, B. Décamps, A. Fraczkiewicz, T. Jourdan, F. Prima, M. Loyer-Prost, Acta Materialia 212 (2021) 116874.
[20] H. Trinkaus, B.N. Singh, A.J.E. Foreman, Journal of Nuclear Materials 199 (1992) 1–5.
[21] C.H. Woo, B.N. Singh, Philosophical Magazine A 65 (1992) 889–912.
[22] R.E. Stoller, M.B. Toloczko, G.S. Was, A.G. Certain, S. Dwaraknath, F.A. Garner, Nuclear Instruments and Methods in Physics Research Section B: Beam Interactions with Materials and Atoms 310 (2013) 75–80.
[23] J.-P. Crocombette, C. Van Wambeke, EPJ Nuclear Sci. Technol. 5 (2019) 7.
[24] B. Horváth, R. Schäublin, Y. Dai, Nuclear Instruments and Methods in Physics Research Section B: Beam Interactions with Materials and Atoms 449 (2019) 29–34.
[25] A. Howie, M.J. Whelan, Proceedings of the Royal Society of London. Series A. Mathematical and Physical Sciences 267 (1962) 206–230.
[26] M.H. Loretto, R.E. Smallman, Defect Analysis in Electron Microscopy, Chapman and Hall, New York, 1975.
[27] M.L. Jenkins, Journal of Nuclear Materials 216 (1994) 124–156.
[28] D.M. Maher, M.H. Loretto, A.F. Bartlett, The Philosophical Magazine: A Journal of Theoretical Experimental and Applied Physics 24 (1971) 181–194.

[29] Y. Liao, An Online Book (2006).
[30] R. Bullough, M.H. Wood, D.W. Wells, J.R. Willis, in: Dislocation Modelling of Physical Systems, Pergamon, 1981, pp. 116–141.
[31] D.J. Bacon, F. Gao, Yu.N. Osetsky, Journal of Nuclear Materials 276 (2000) 1–12.
[32] Y.N. Osetsky, D.J. Bacon, Modelling and Simulation in Materials Science and Engineering 11 (2003) 427.
[33] L.E. Seitzman, L.M. Wang, G.L. Kulcinski, R.A. Dodd, Journal of Nuclear Materials 141–143 (1986) 738–742.
[34] Z. Yao, R. Schäublin, M. Victoria, Journal of Nuclear Materials 323 (2003) 388–393.
[35] Y.N. Osetsky, A.V. Barashev, Y. Zhang, Materialia 4 (2018) 139–146.
[36] C. Sun, F.A. Garner, L. Shao, X. Zhang, S.A. Maloy, Nuclear Instruments and Methods in Physics Research Section B: Beam Interactions with Materials and Atoms 409 (2017) 323–327.
[37] F.A. Garner, J. Wang, L. Shao, S.A. Maloy, V.A. Pechenkin, Conference IWSMT-13 (2016) Chattanooga TN.
[38] G.S. Was, T. Allen, Journal of Nuclear Materials 205 (1993) 332–338.
[39] N. Khiara, F. Onimus, L. Dupuy, W. Kassem, J.-P. Crocombette, T. Pardoen, J.-P. Raskin, Y. Bréchet, Journal of Nuclear Materials 541 (2020) 152336.